Electronic supplementary information (ESI)

# A breathable inorganic-organic interface for fabricating a crack-free nickel-rich cathode with long-term stability

Yipeng Sun[1]‡, Jinjin Ma[1]‡, Duojie Wu[3]‡, Changhong Wang[1,3], Yang Zhao[1], Matthew Zheng[1], Ruizhi Yu[1], Weihan Li[1], Minsi Li[1], Yingjie Gao[1], Xiaoting Lin[1], Hui Duan[1], Jiamin Fu[1], Zhiqiang Wang[2], Ruying Li[1], M. Danny Gu [3]*, Tsun-Kong Sham[2]*, Xueliang Sun[1,3]*

[1] Department of Mechanical and Materials Engineering,
University of Western Ontario, London, Ontario, N6A 5B9, Canada
*E-mail: xsun9@uwo.ca (X.L. Sun)*
[2] Department of Chemistry,
University of Western Ontario, London, Ontario, N6A 5B7, Canada
*E-mail: tsham@uwo.ca (T.K. Sham)*

[3]Eastern Institute for Advanced Study,

Eastern Institute of Technology, Ningbo, Zhejiang, 315200, P.R. China

*E-mail: m.danny.gu@gmail.com*

‡These authors contributed equally to this work.

## Experimental

Coating procedure: $LiNi_{0.94}Co_{0.05}Mn_{0.01}O_2$ was purchased from GEM Co., Ltd. and used as received for the MLD modification. The deposition procedure is conducted by an Arradiance GEMstar-8 ALD system. The precursors used for the deposition of hybrid polyurea (HPU) coating are 1,4 – phenylene diisocyanate (PDIC), ethylenediamine (ED), and trimethylaluminum (TMA). The MLD procedure of HPU followed our previously reported work. The MLD chamber was heated and kept at 65 ˚C for the deposition. The pressure of the chamber was maintained at ~ 300 mTorr. Each of the precursor is placed in separate stainless steel container to prevent air and moisture exposure. ED and TMA were kept at room temperature, while PDIC was kept at 90 ˚C to supply sufficient evaporation pressure. Argon gas was introduced as both carrier gas and purging gas. The pulse periods for TMA, ED, PDIC are 100 ms, 200 ms, and 1000 ms, respectively. A complete MLD cycle of HPU can be described as TMA pulse/purge/ED pulse/purge/PDIC pulse/purge/ED pulse/purge for periods of 0.1/50/0.2/50/1/50/0.2/50 s. Ni94 powder was coated by different number of MLD HPU cycles (2, 4, 10, 20 cycles) and denoted as 94@H2, 94@H4, 94@H10, and 94@H20.

Electrochemical measurements: The Ni94 powder was mixed with poly(vinylidene difluoride) (PVDF), vapor grown carbon fiber (VGCF), carbon black (CB), with a Ni94:PVDF:VGCF:CB ratio of 90:5:2.5:2.5. The mixture was then thoroughly dispersed in N-methylpyrrolidone (NMP) and formed a uniform slurry, which was then casted on aluminum foil and dried at 110 °C overnight. The cathodes were cut into disks with a diameter of 10 mm and weighed. The areal loading of active material was ~5.0 mg $cm^{-2}$. To assemble 2032-type coin cells, the cathode disks were transferred into an argon filled glovebox with sub ppm level of oxygen and water. Lithium foils were used as counter electrodes and the separators were Celgard 2400 Polypropylene. The electrolyte was 1 M $LiPF_6$ dissolved in a mixed solvent of 1:1:1 EC/DEC/DMC. Galvanostatic charge/discharge tests were conducted at Neware battery testing system, the voltage range for cycling is from 2.8 V to 4.3 V (vs $Li^+$/Li), and all the testing is performed at room temperature. The electrochemical impedance spectrum (EIS) was tested using versatile multichannel potentiostat 3/Z (VMP3) at a frequency range of $10^{-1}$ – $10^6$ Hz. The electrochemical tests were carried out at room temperature. The electronic conductivity was measured by direct current (DC) polarization technique. The cathode powder was transferred to a polytetrafluoroethylene (PTFE) die and pressed by stainless steel rods on both sides to obtain a pallet for electronic conductivity testing. The cells were applied under a series of DC voltages (0.05 V, 0.1 V, 0.15V, 0.2 V, 0.25V) for 1 hour at each voltage and the currents were recorded. The ionic conductivity was also tested by DC polarization technique. The cathode pallets were also sandwiched by electron blocking solid electrolytes to obtain the current exclusively from the ionic transport. The cells were applied under a series of DC voltages (0.05 V, 0.1 V, 0.15V, 0.2 V, 0.25V) for 1 hour at each voltage and the currents were recorded. The resistance of the pallets was calculated by ohm's law.

Materials characterization: The crystal structure of Ni94 was characterized by X-ray Diffraction (XRD) using a D8 ADVANCE (XRD) diffractometer with a Cu Kα X-ray source in the range of 10-80° with a step of 0.01 ° per second. Scanning electron microscopy (SEM) images and energy dispersive X-ray spectroscopy (EDS) mapping were obtained by a Hitachi 4800N scanning electron microscope equipped with an EDS detector. The working voltage for EDS mapping was 20 kV. For post-cycling characterization, the coin cells were disassembled in the Argon filled glovebox and the cathode is carefully taken out. The electrodes were washed by DEC for several times to remove any residue Li salt in the electrolyte before any characterization. The surface and depth profile was characterized by TOF-SIMS IV (ION-TOF GmbH, Germany) with 25 keV of $Bi_3^+$ primary ion beam. The secondary ions are generated by sputtering the sample surface using 3 keV $Cs^+$ ions. Depth profiles of secondary ions were obtained on an area of $150 \times 150$ $\mu m^2$. XANES measurements for Ni K-edge and Co K-edge were conducted at soft X-ray Micro characterization Beamline (SXRMB) end station at the Canadian Light Source (CLS). Synchrotron-based powder diffraction results were measured at the Brockhouse High Energy Wiggler beamline at the Canadian Light Source (CLS) using a wavelength of 0.2038 Å. The Ni L-edge spectra were recorded at the CLS Spherical Grating Monochromator (SGM) beamline. The spectra were firstly normalized to the incident photon flux for analysis. High-angle annular dark field-scanning transmission electron microscopy (HAADF-STEM) images, Energy dispersive X-ray spectroscopy (EDS) mapping, and selected area electron diffraction (SAED) patterns were collected by a Cs-corrected Titan Themis G2 300 TEM, which is performed at 300 kV and coupled with a Bruker Quantax Super –X EDS detector. The cycled cathodes were scraped off from the current collector, well dispersed in hexane under ultrasonic and coated on a TEM Cu grid. Focused ion beam (FIB) milling was conducted to thin the cathode particles to a suitable thickness for TEM and realize the cross-section morphology.

Theoretical Section: Quantum chemistry calculations were first performed to optimize molecular geometries of PU and HPU molecules using the Gaussian 16 package at B3LYP/6-31G(d) level of theory (the B3LYP hybrid functional and the 6-31G(d) basis set), and thereafter to calculate the corresponding HOMO-LUMO energies based on their optimized molecular structures. The possible sites for Li ion adsorption is obtained based on the electrostatic potential (ESP) density of PU and HPU. The binding energy is calculated by using the energy of Li on the coating to subtract the energy of coating and then subtract the energy of Li.

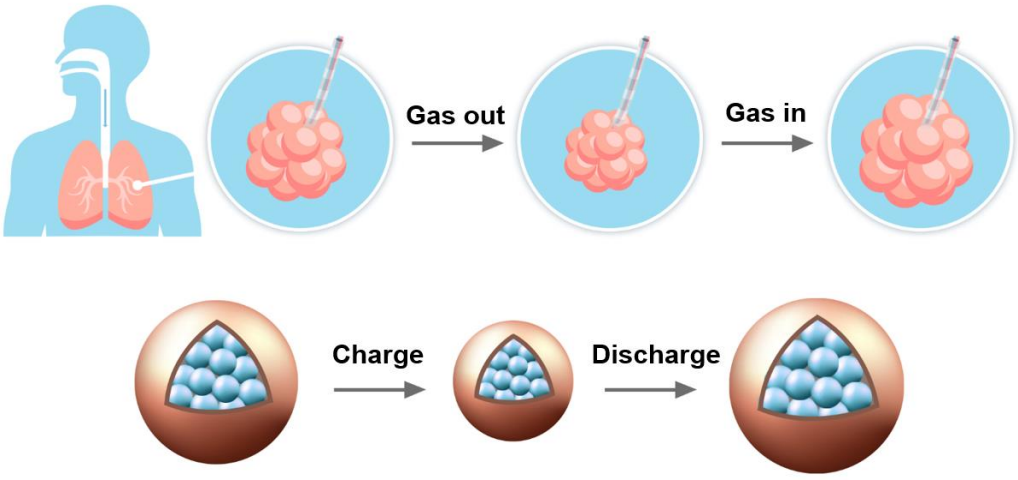


Figure S1. Schematic showing working mechanism of alveoli from human lung and breathable Ni-rich cathode.

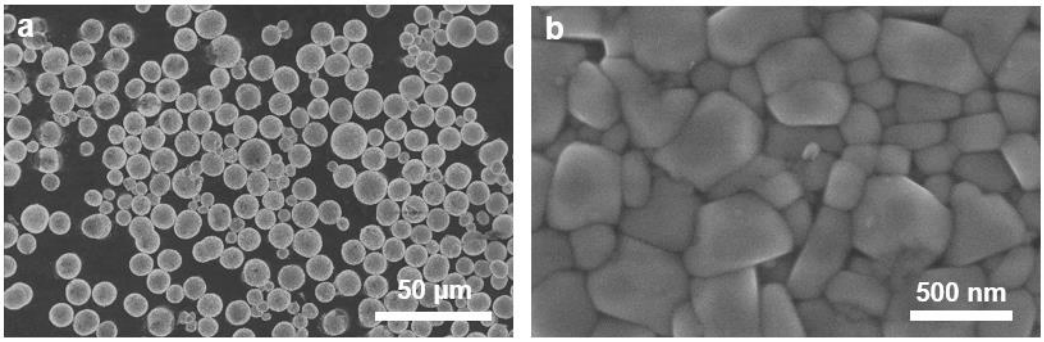


Figure S2. SEM image of Ni94 cathode particles under (a) low and (b) high magnification.

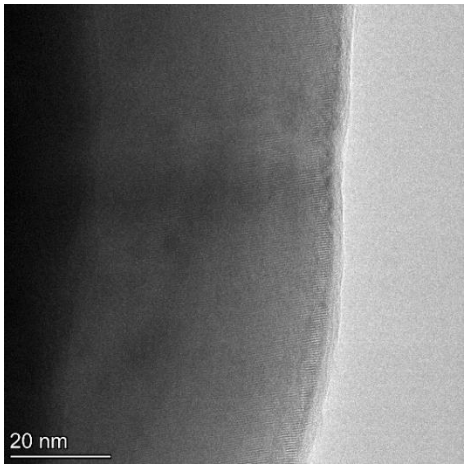


Figure S3. TEM image of 94@H10 cathode showing HPU coating on the cathode particle.

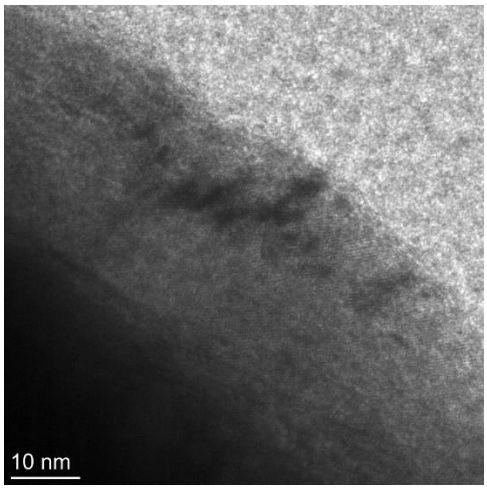


Figure S4. TEM image of pristine Ni94 cathode.

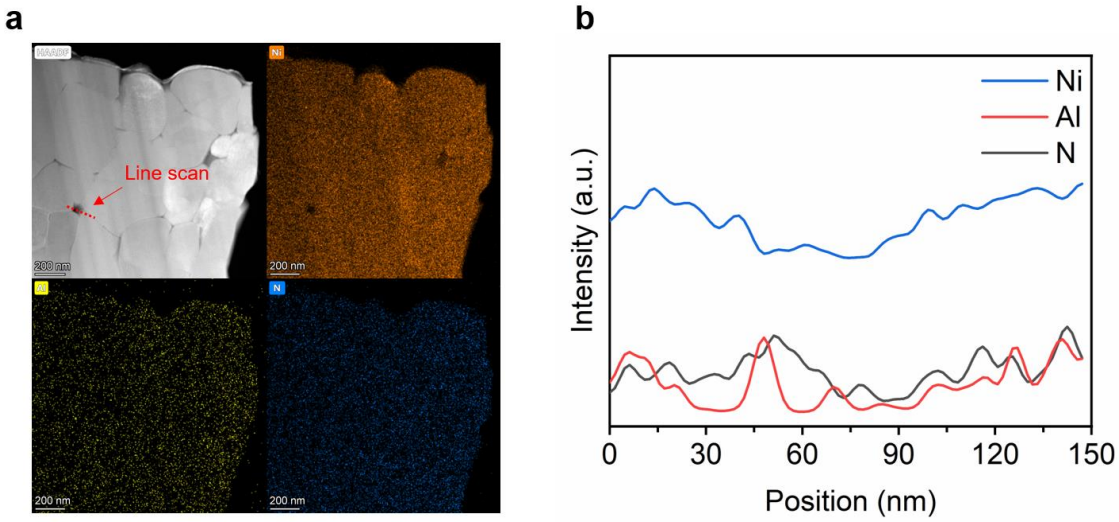


Figure S5. (a) TEM image and EDS mapping for Ni, Al, and N elements on a cross-section of 94@H10 particle. (b) Corresponding linear scan results.

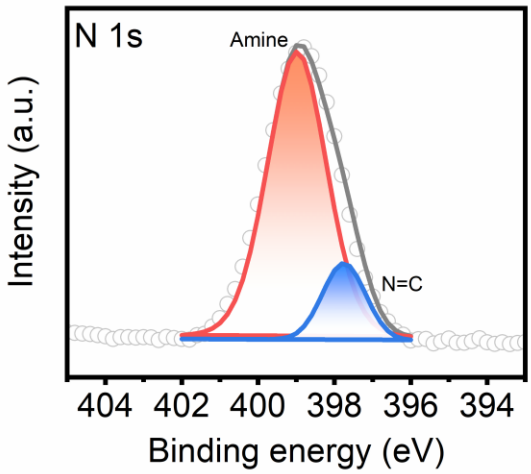


Figure S6. XPS N 1s spectrum of 94@H10.

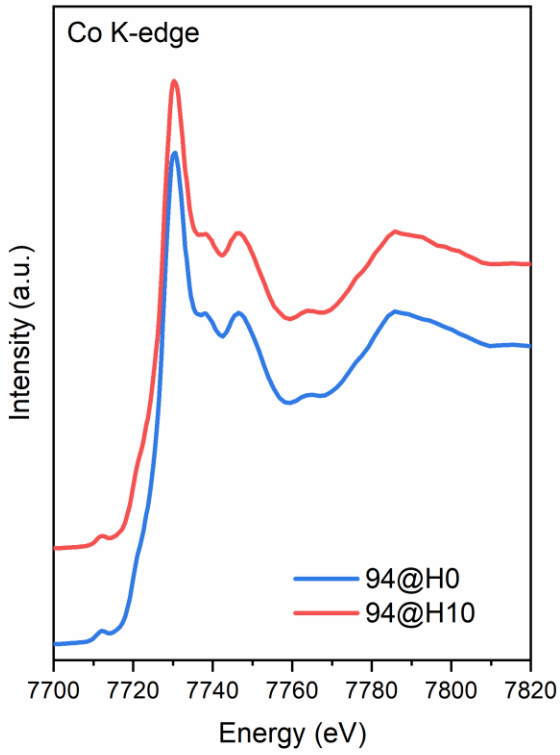


Figure S7. Co K-edge XANES spectra of 94@H0 and 94@H10.

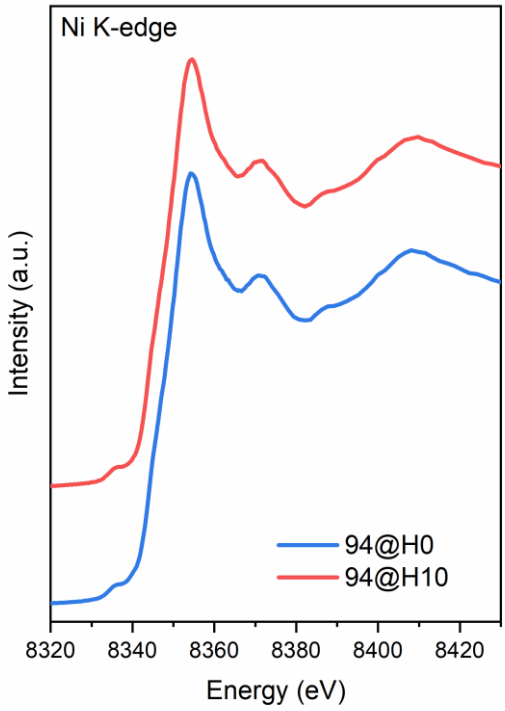


Figure S8. Ni K-edge XANES spectra of 94@H0 and 94@H10.

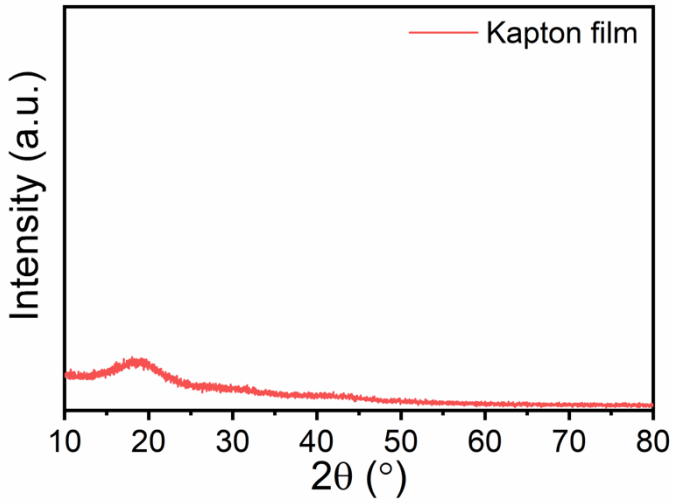


Figure S9. XRD pattern of Kapton film.

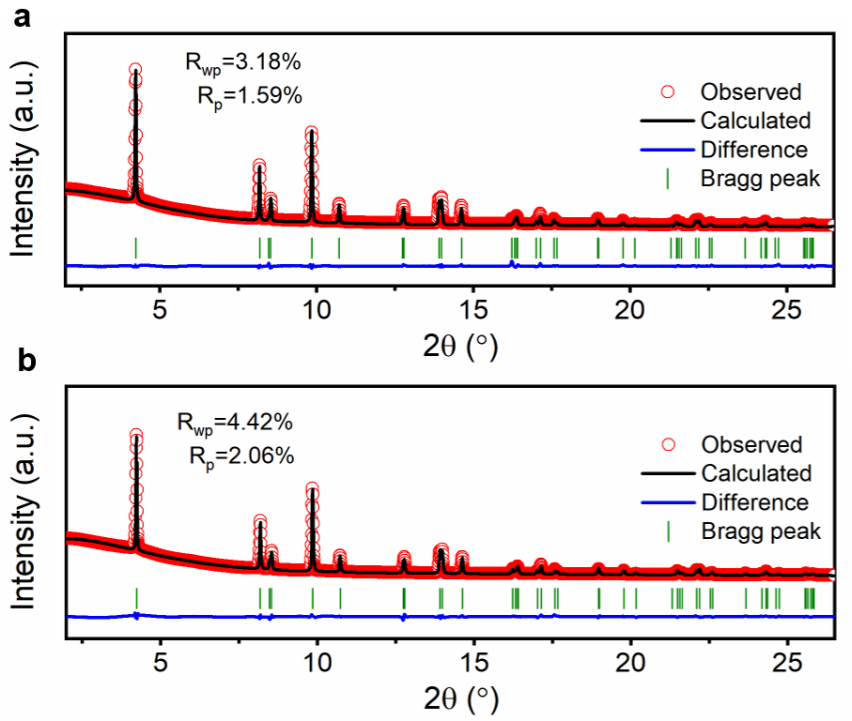


Figure S10. SXRD pattern and refinement results for a (a) 94@H0 and (b) 94@H10.

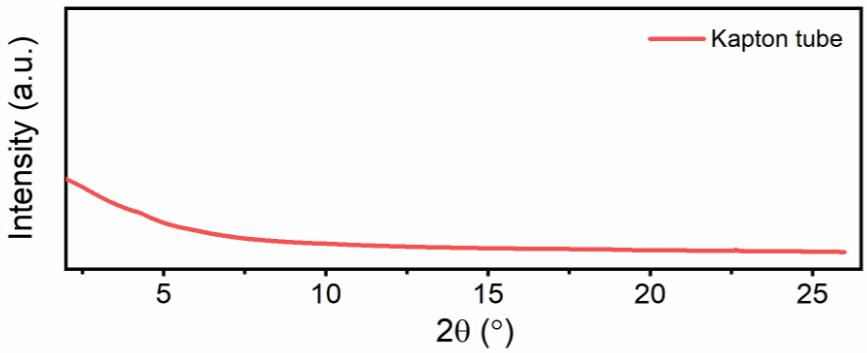


Figure S11. SXRD pattern of Kapton tube.

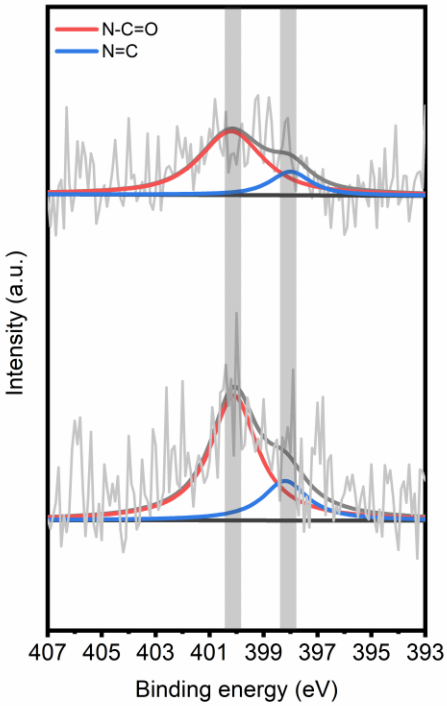


Figure S12. Synchrotron-based high energy XPS spectra of N 1s at different photo energies (3000 eV on the top and 7000 eV at bottom).

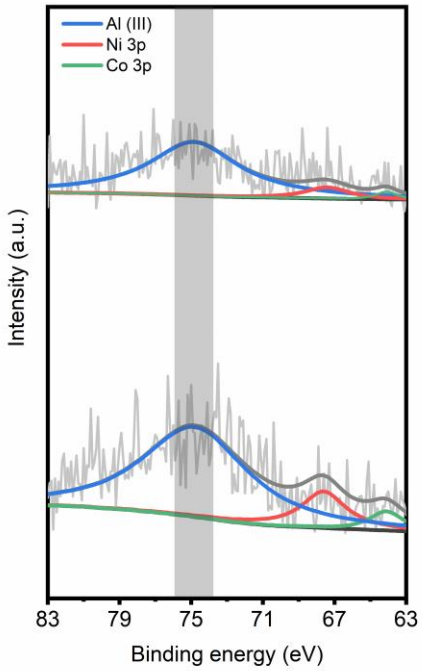


Figure S13. Synchrotron-based high energy XPS spectra of Al 2p, Ni 3p, and Co 3p at different photo energies (3000 eV on the top and 7000 eV at bottom).

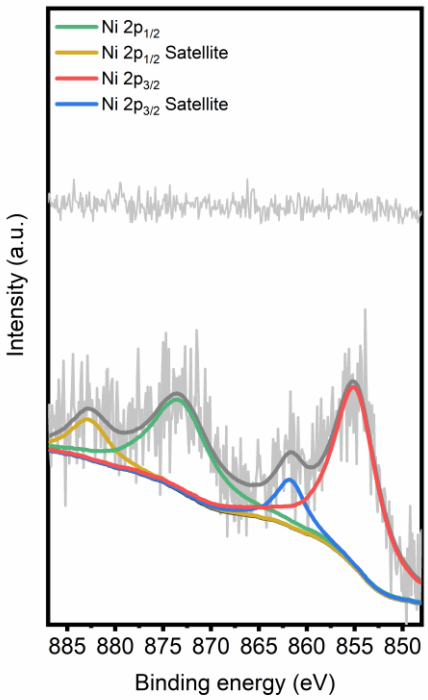


Figure S14. Synchrotron-based high energy XPS spectra of Ni 2p at different photo energies (3000 eV on the top and 7000 eV at bottom).


Figure S15. Optical images showing a single droplet of the carbonate electrolyte on the surface of (a)94@H0 electrode (b)94@H10 electrode.

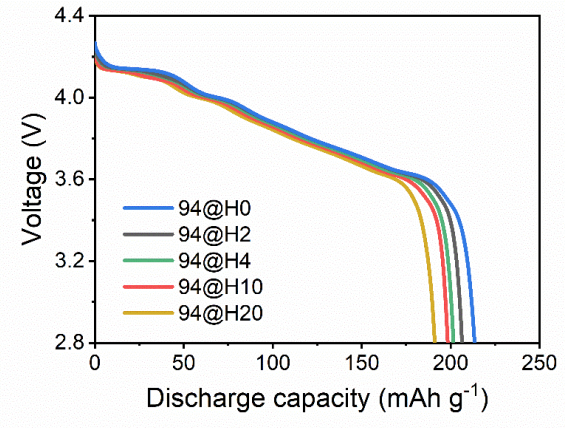


Figure S16. Initial discharge voltage profile of Ni94 cathode with different MLD cycles showing the influence in the capacity upon MLD coating.

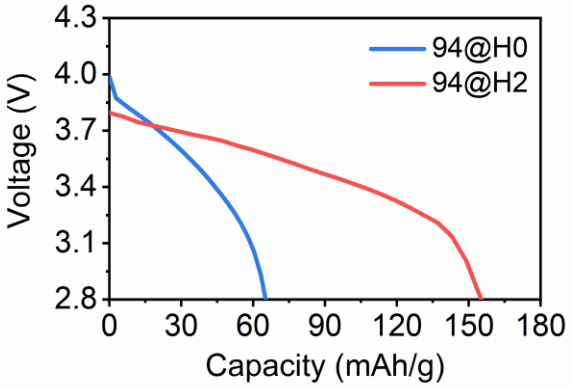


Figure S17. Discharge voltage profiles for 94@H0 and 94@H2 cycling at 10 C.

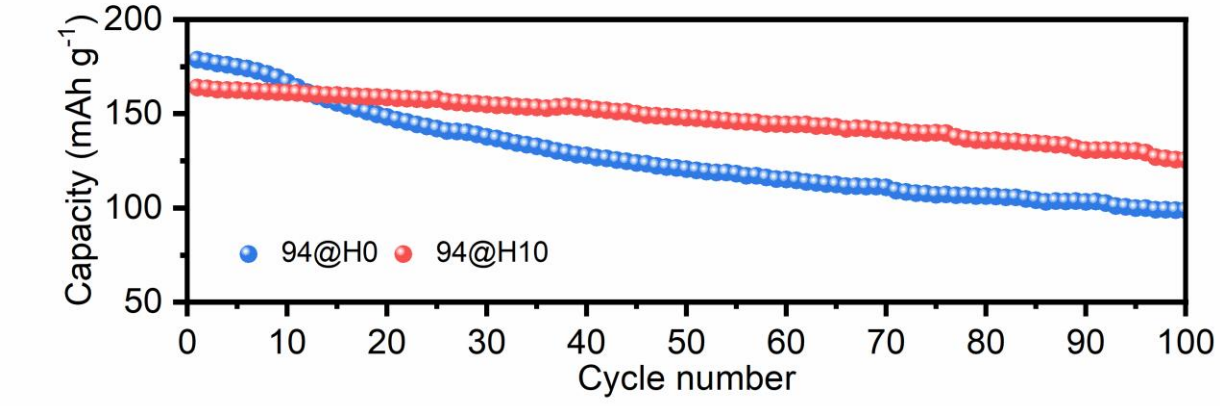


Figure S18. Cycling performances of 94@H0 and 94@H10 at 5C for a voltage range of 2.8-4.3 V.

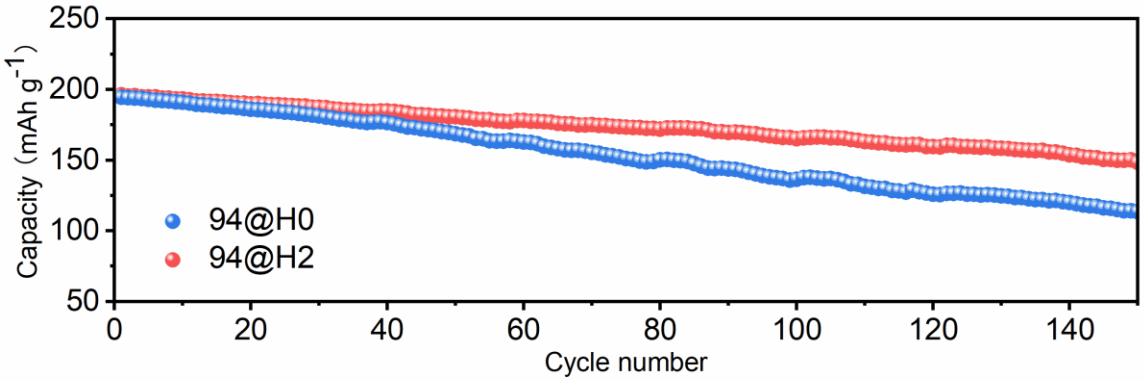


Figure S19. Cycling performances of 94@H0 and 94@H2 at 2C for a voltage range of 2.8-4.5 V.

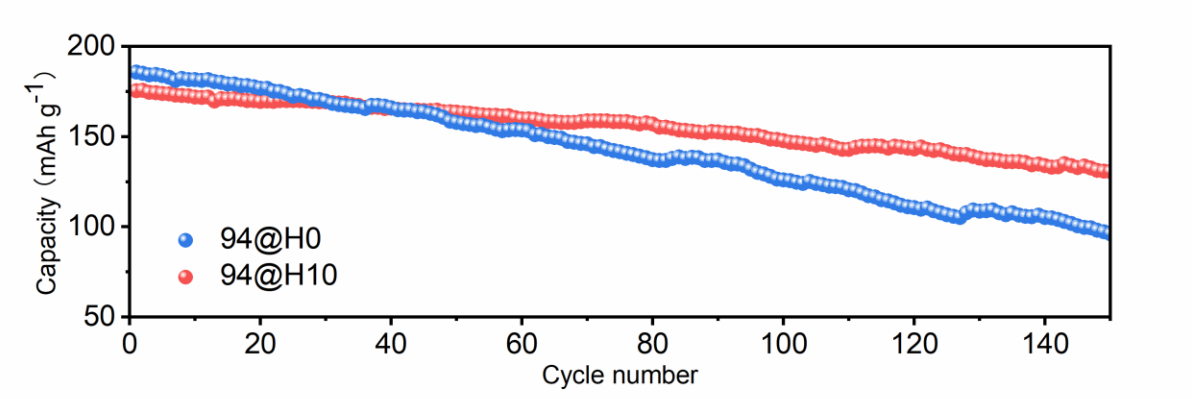


Figure S20. Cycling performances of 94@H0 and 94@H10 at 5C for a voltage range of 2.8-4.5 V.

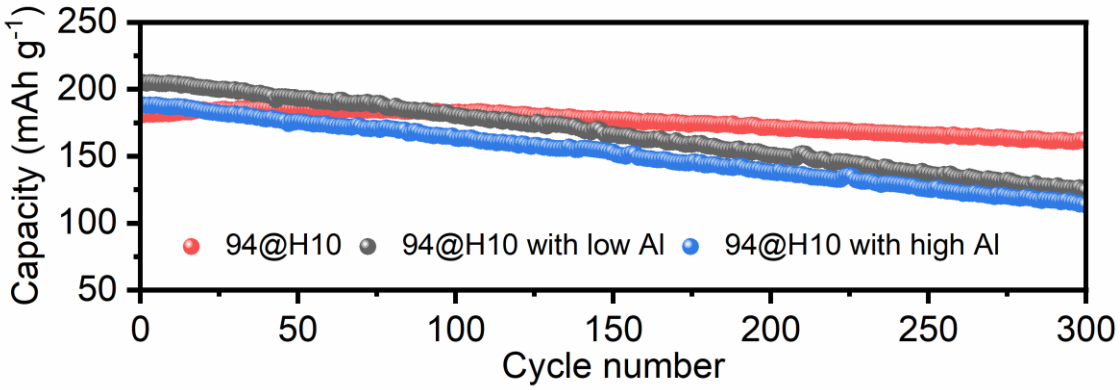


Figure S21. Cycling performance with different Al percentage in MLD coating. During the MLD procedure, 50 ms of TMA was pulsed for '94@H10 with low Al'; and 100 ms of TMA was pulsed for 94@H10; and 200 ms of TMA was pulsed for '94@H10 with high Al'.

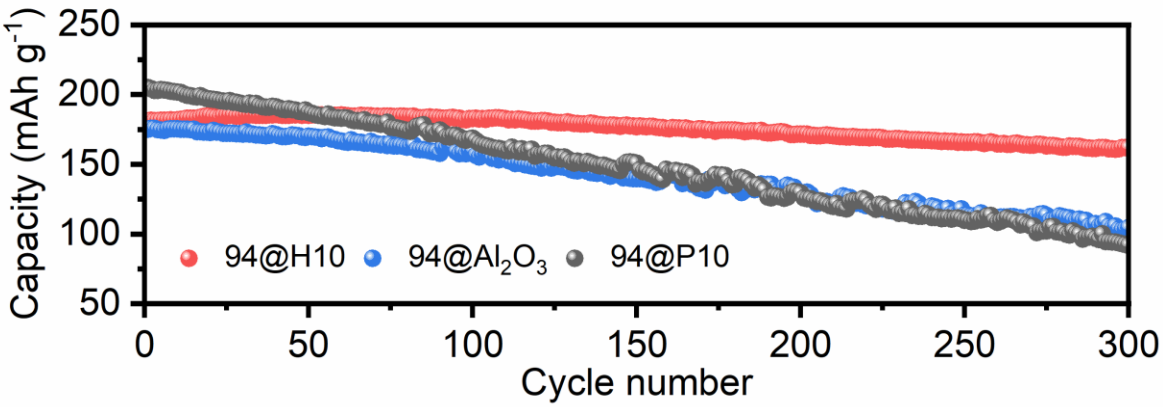


Figure S22. Cycling performance comparing ALD $Al_2O_3$ coated Ni94 (94@$Al_2O_3$) and 10 MLD cycles of organic PU coated Ni94 (94@P10).

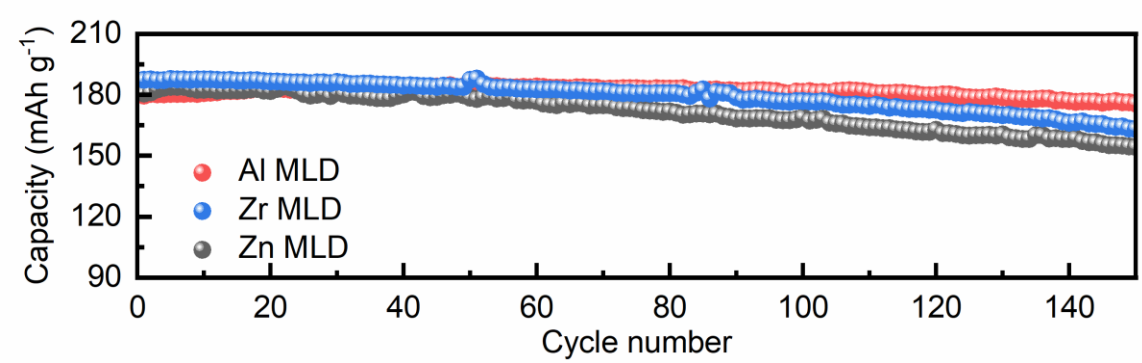


Figure S23. Cycling performance comparing different metals in hybrid PU coating.

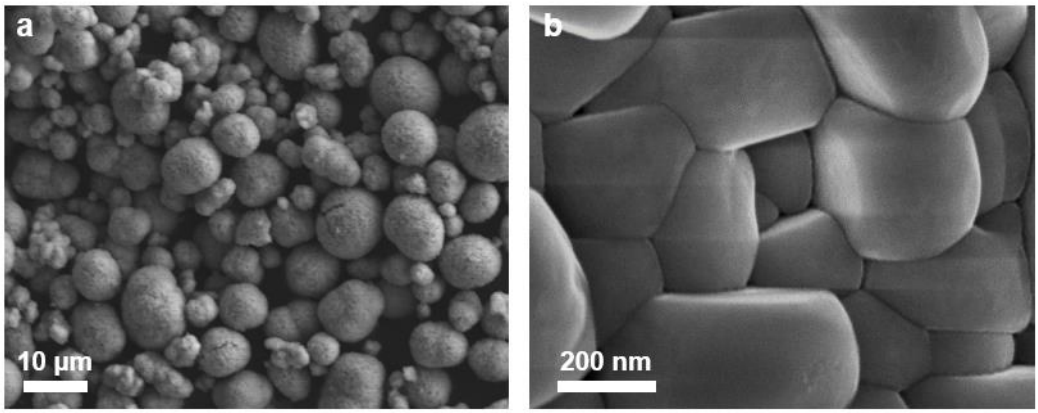


Figure S24. SEM image of NMC811 cathode particles under (a) low and (b) high magnification.

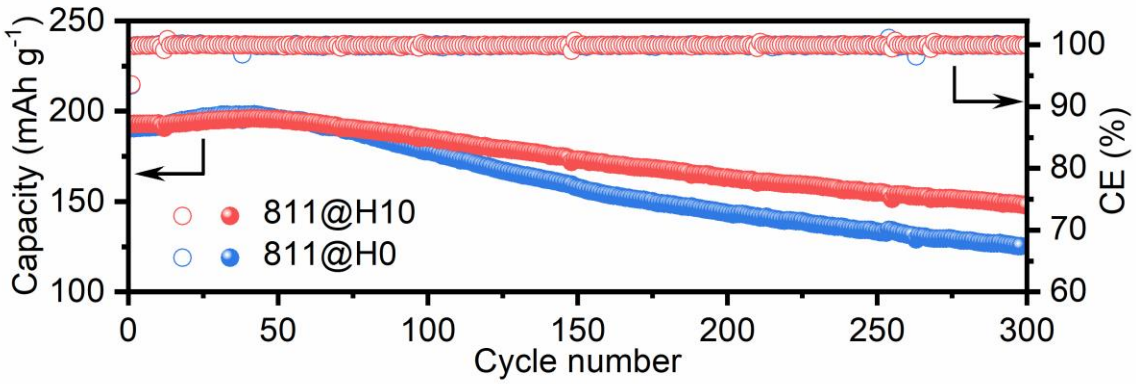


Figure S25. Cycling performance of NMC811 cathode showing the universal application of MLD strategy.

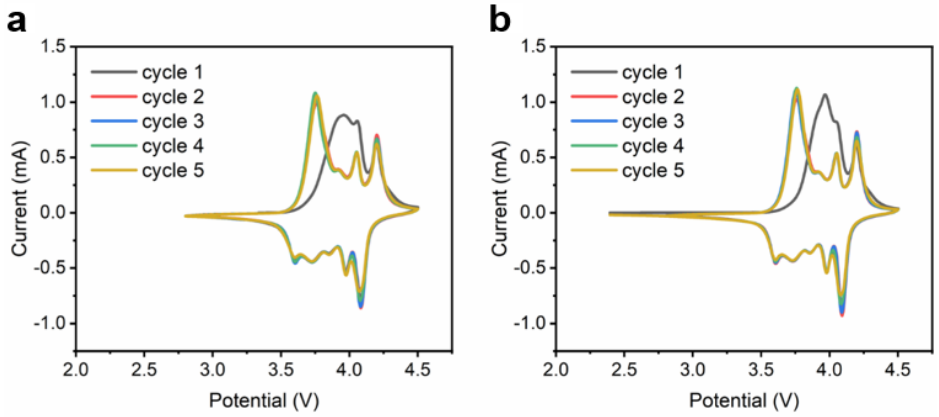


Figure S26. CV curves for the initial 5 cycles in the voltage range of 2.8 V to 4.5 V for (a) 94@H0 and (b) 94@H10.

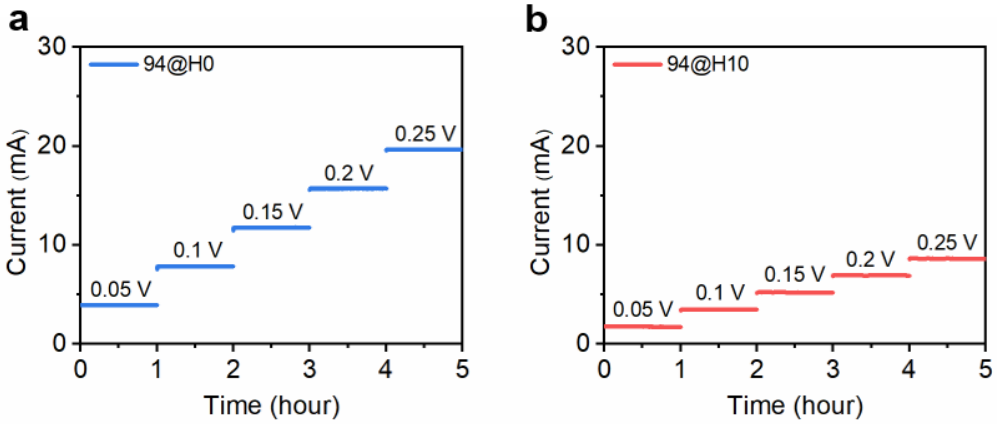


Figure S27. The recorded currents from electronic conductivity measurement for (a) 94@H0 and (b) 94@H10.

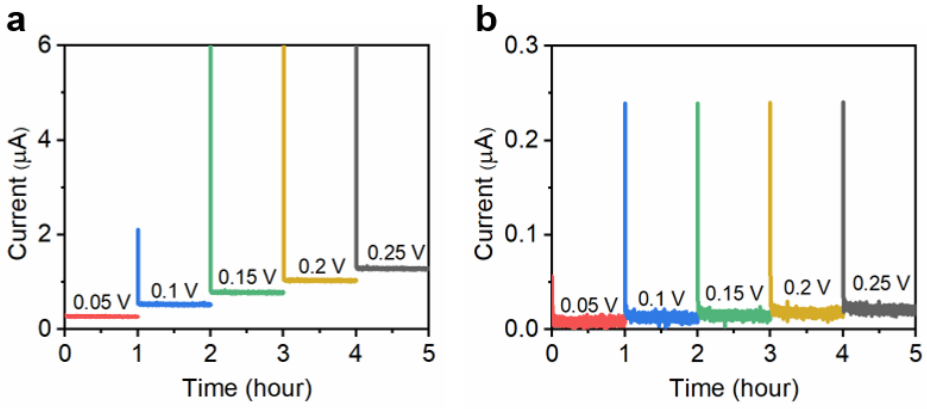


Figure S28. The recorded currents from ionic conductivity measurement for (a) 94@H0 and (b) 94@H10.

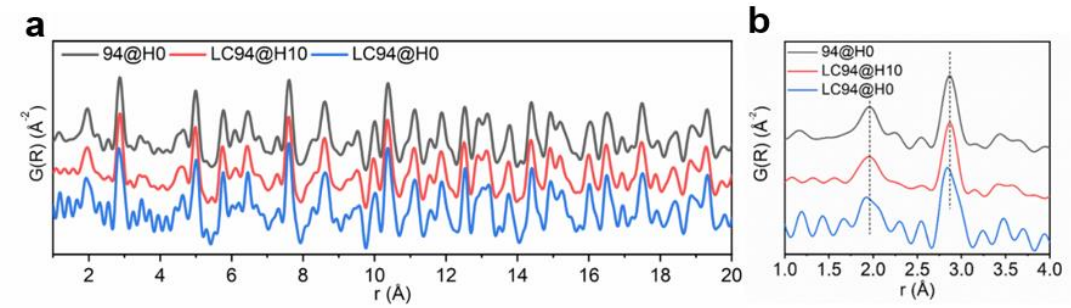


Figure S29. PDF patterns of 94@H0, LC94@H0 and LC94@H10.

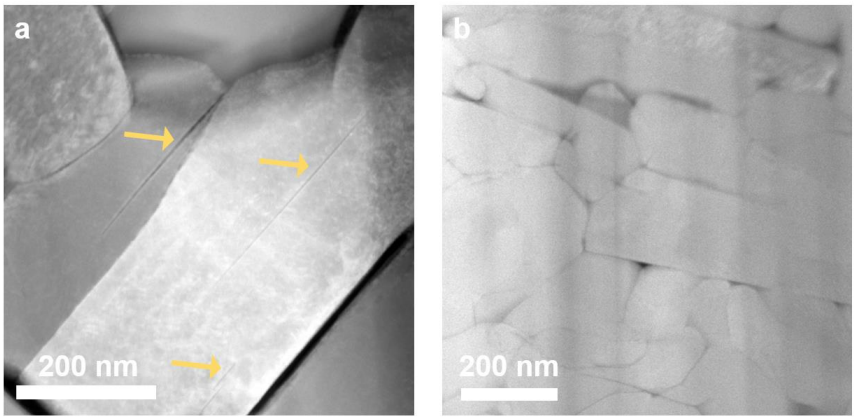


Figure S30. TEM images showing the cross-section of (a) LC94@H0 and (b) LC94@H10.

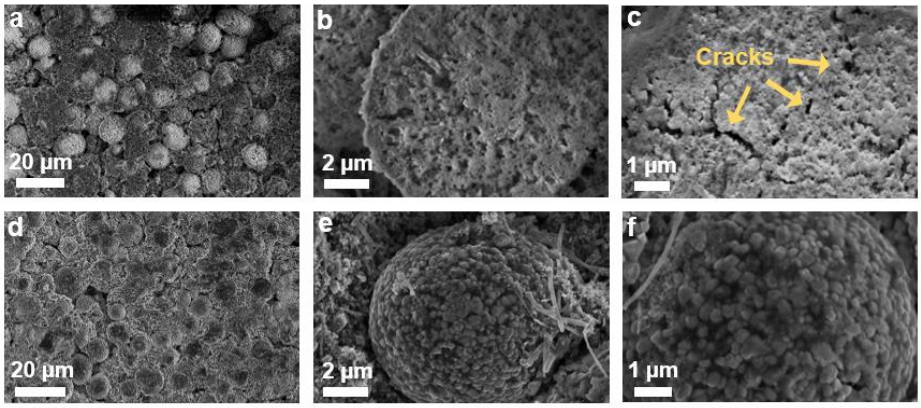


Figure S31. SEM images of (a-c) 94@H0 and (d-f) 94@H10 at different magnifications after cycling, respectively.

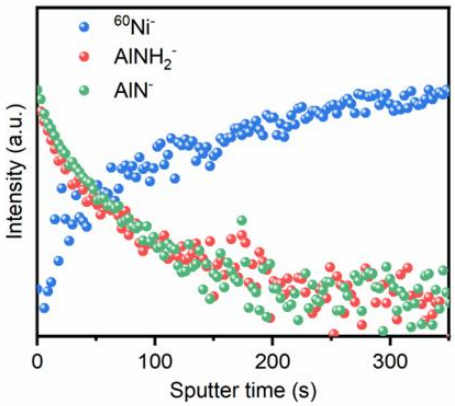


Figure S32. TOF-SIMS depth profiles of $^{60}Ni^-$, $AlNH_2^-$, and $AlN^-$ secondary ions generated from LC94@H10.

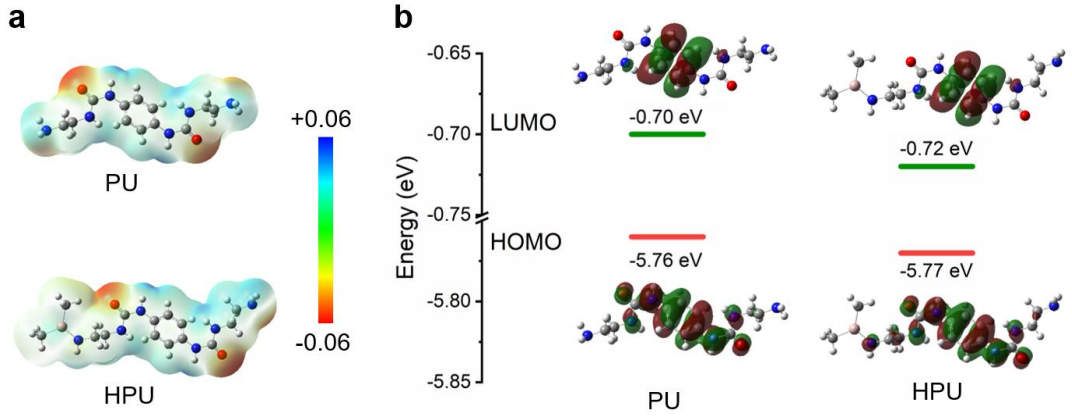


Figure S33. (a) Simulated ESP distributions of HPU and PU. (b) Calculated the highest occupied molecular orbital (HOMO) and lowest unoccupied molecular orbital (LUMO) energy values.

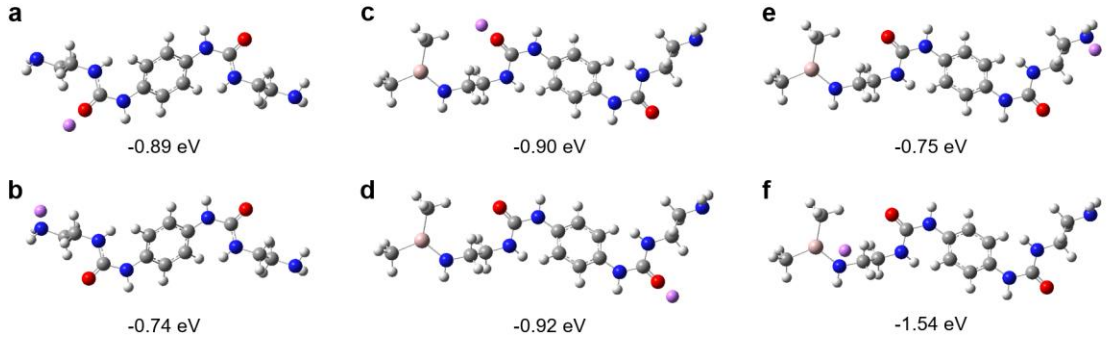


Figure S34. Li binding energy calculation results for PU and HPU. (a) O site of PU. (b) N site of PU. (c) O site 1 of HPU. (d) O site 2 of HPU. (e) N site 1 of HPU. (f) N site 2 of HPU.

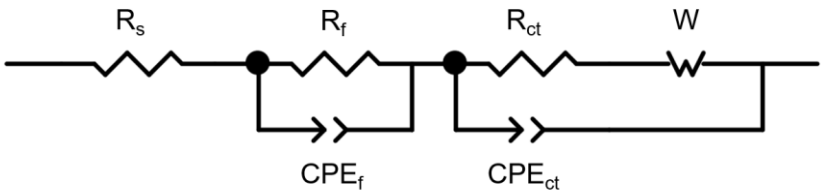


Figure S35. Equivalent circuit for the EIS fitting of 94@H0 and 94@H10.

Table S1. Summary of R factors and lattice parameters of 94@H0 and 94@H10 from synchrotron-based XRD Rietveld refinements.

| Sample | a (Å) | c (Å) | V ($Å^3$) | Rwp / % | Rp / % | Ni in Li site / % |
|---|---|---|---|---|---|---|
| 94@H0 | 2.8713(8) | 14.1846(2) | 101.276 | 3.18 | 1.59 | 7.57 |
| 94@H10 | 2.8705(1) | 14.1736(5) | 101.142 | 4.42 | 2.06 | 5.83 |

Table S2. Summary of performance reported in the literatures for Ni-rich cathode with Ni content over 0.88.

| Cathode | Strategy | Voltage range | Cycling current | Capacity retention | Energy density | Refence |
|---|---|---|---|---|---|---|
| $Li_{1.06}(Ni_{0.88}Co_{0.06}Mn_{0.06})_{0.94}O_2$ | $TiNb_2O_7$ coating | 3.0-4.3 V | 1 C | 87.2% for 200 cycles | 518 Wh $kg^{-1}$ after 200 cycles | Nano Energy 2022, 91, 106665 |
| $Li[Ni_{0.88}Co_{0.1}Al_{0.02}]O_2$ | Al doping | 2.7-4.3 V | 0.5 C | 91.9% for 100 cycles | 578 Wh $kg^{-1}$ after 100 cycles | Energy Environ. Sci. 2021,14, 5084-5095 |
| Single-crystal $LiNi_{0.88}Co_{0.09}Mn_{0.03}O_2$ | $Li_{1.4}Y_{0.4}Ti_{1.6}(PO_4)_3$ coating | 2.75-4.4 V | 0.5 C | 86.5% for 200 cycles | 617 Wh $kg^{-1}$ after 200 cycles | Nat. Commun. 2021, 12, 5320 |
| $LiNi_{0.9}Co_{0.05}Mn_{0.05}O_2$ | Perovskite $La_4NiLiO_8$ coating | 2.8-4.3 V | 1 C | 92.6% for 100 cycles | 528 Wh $kg^{-1}$ after 100 cycles | Adv. Mater. 2023, 35, 2209483. |
| $Li[Ni_{0.90}Co_{0.05}Mn_{0.05}]O_2$ | B doping | 2.7-4.3 V | 0.5 C | 91.0% for 100 cycles | 591 Wh $kg^{-1}$ after 200 cycles | Adv. Energy Mater. 2018, 1801202 |
| $Li[Ni_{0.90}Co_{0.06}Mn_{0.04}]O_2$ | $Li_2CO_3$ coating | 3.0-4.3 V | 1 C | 89.5% for 100 cycles | 578 Wh $kg^{-1}$ after 200 cycles | Adv. Mater. 2022, 2108947 |
| $LiNi_{0.9}Co_{0.05}Mn_{0.05}O_2$ | Nb coating/ substitution | 2.8-4.4 V | C/3 | 93.5% for 200 cycles | 608 Wh $kg^{-1}$ after 200 cycles | Chem. Mater. 2022, 34, 17, 7858–7866 |
| $LiNi_{0.94}Co_{0.03}Mn_{0.03}O_2$ | B doping and $BPO_4$ coating | 2.7-4.3 V | 0.5 C | 90.8% for 100 cycles | 608 Wh $kg^{-1}$ after 100 cycles | J. Mater. Chem. A 2020,8, 21306-21316 |
| $Li_{1-m}(Ni_{0.94}Al_{0.06})_{1+m}O_2$ | long-range cationic disordering | 2.7-4.3 V | 1 C | 96% for 100 cycles, ~75.9% for 300 cycles | 535 Wh $kg^{-1}$ after 100 cycles<br>407 Wh $kg^{-1}$ after 300 cycles | Angew. Chem. Int. Ed. 2023, 62, e202214880 |
| $LiNi_{0.94}Co_{0.03}Mn_{0.03}O_2$ | MLD | 2.8-4.3 V | 0.5C | 94.7% for 200 cycles | 616 Wh $kg^{-1}$ after 100 cycles<br>585 Wh $kg^{-1}$ after 200 cycles<br>492 Wh $kg^{-1}$ after 500 cycles | Our work |

Table S3. Fitting results showing charge transfer resistance and CEI resistance after cycling.

| Cycles | After 20 cycles | | | After 50 cycles | | |
|---|---|---|---|---|---|---|
| Samples | $R_s$ (Ω) | $R_f$ (Ω) | $R_{ct}$ (Ω) | $R_s$ (Ω) | $R_f$ (Ω) | $R_{ct}$ (Ω) |
| 94@H0 | 7.201 | 7.183 | 81.22 | 6.248 | 9.173 | 155.7 |
| 94@H10 | 6.582 | 6.541 | 72.72 | 7.668 | 7.312 | 112.5 |